

Comparative study of the structural and magnetic properties of $\text{Mn}_{1/3}\text{NbS}_2$ and $\text{Cr}_{1/3}\text{NbS}_2$ A. E. Hall ^{1,*}, J. C. Loudon,² P. A. Midgley ², A. C. Twitchett-Harrison,² S. J. R. Holt ¹, D. A. Mayoh ¹,
J. P. Tidey ³, Y. Han,¹ M. R. Lees ¹ and G. Balakrishnan ^{1,†}¹*Department of Physics, University of Warwick, Coventry, CV4 7AL, United Kingdom*²*Department of Materials Science and Metallurgy, University of Cambridge, 27 Charles Babbage Road, Cambridge, CB3 0FS, United Kingdom*³*Department of Chemistry, University of Warwick, Coventry, CV4 7AL, United Kingdom*

(Received 5 October 2021; revised 10 January 2022; accepted 28 January 2022; published 23 February 2022)

We compare the magnetism of single crystals of the intercalated transition metal dichalcogenides $\text{Cr}_{1/3}\text{NbS}_2$ and $\text{Mn}_{1/3}\text{NbS}_2$ using techniques such as dc and ac susceptibility and Lorentz transmission electron microscopy (LTEM). We present a detailed structural investigation of these materials using electron and single-crystal x-ray diffraction measurements to show how substitutional disorder and stacking faults can manifest in $\text{Cr}_{1/3}\text{NbS}_2$ and $\text{Mn}_{1/3}\text{NbS}_2$, and give rise to additional superlattice reflections in diffraction patterns acquired from $\text{Mn}_{1/3}\text{NbS}_2$. Magnetic susceptibility and LTEM measurements show $\text{Cr}_{1/3}\text{NbS}_2$ displays chiral helimagnetism below its magnetic ordering temperature (T_C) of 111 K, while there is no evidence that $\text{Mn}_{1/3}\text{NbS}_2$ exhibits helimagnetic ordering below its transition temperature $T_C = 45$ K.

DOI: [10.1103/PhysRevMaterials.6.024407](https://doi.org/10.1103/PhysRevMaterials.6.024407)

I. INTRODUCTION

Chiral lattices break symmetry in such a way that they cannot be superimposed onto their mirror image. In certain chiral-lattice magnets, a helicoidal magnetic winding can be stabilized due to competition between the symmetric ferromagnetic exchange interaction, which preferentially aligns the magnetic moments parallel to one another, and the anti-symmetric Dzyaloshinskii-Moriya interaction (DMI), which preferentially aligns magnetic moments perpendicular to their neighbors [1–3]. In select materials, applying an external magnetic field perpendicular to the helical axis stabilizes spin structures such as skyrmions [4] or a chiral soliton lattice (CSL) [5,6].

The CSL can be described as regions of moments which are ferromagnetically aligned with the external field and separated by 360° domain walls (see Fig. 1). As the applied field is increased, the extent of these ferromagnetic regions, and thus the period of the CSL, are increased, until eventually the moments are aligned in a field polarized state. The CSL is robust to deformation [5,7] from factors such as thermal fluctuations or material defects, and therefore of considerable interest for spintronic applications [8]. One known CSL host is $\text{Cr}_{1/3}\text{NbS}_2$, a member of a family of hexagonal layered transition metal dichalcogenides (TMDCs) intercalated with $3d$ transition metals that occupy octahedral $2c$ or $2d$ Wyckoff positions [9] between the trigonal prismatic layers (see Fig. 2). The layers are bonded by weak van der Waals forces, allowing for easy twisting of layers relative to each other, causing the common stacking faults that are observed in these materials.

These intercalated TMDCs can be represented by the formula $M_{1/3}XY_2$, where $X = \text{Nb, Ta}$; $Y = \text{S, Se}$; and M is the intercalated transition metal. Depending on the type of transition metal used as the intercalant, the final compound can display many different types of magnetism [8,10]. The crystal structures of these materials are highly dependent on the level of intercalant, with the pristine XY_2 compound forming in the centrosymmetric $P6_3/mmc$ space group and transforming to the noncentrosymmetric space group $P6_322$ above a critical concentration of the intercalant, which occurs at $M_{1/3}XY_2$. At this point, the majority of the intercalating atoms occupy a single $2c$ or $2d$ Wyckoff position rather than being equally shared between the two sites as would be the case for the centrosymmetric space group [11]. It is this transition to the noncentrosymmetric structure that gives rise to the DMI and thus helps stabilize an ordered chiral helimagnetic state. This change in space group is accompanied by specific changes to the magnetic transition temperature of the material, and sometimes even changes to the type of magnetic ordering present [8].

$\text{Cr}_{1/3}\text{NbS}_2$ is a well-studied material that displays a helical magnetic ground state below its magnetic ordering temperature $T_C = 127\text{--}130$ K [12–15]. Disorder effects in this material have been shown to suppress the magnetic transition temperature to values as low as $T_C = 88$ K [16]. It has a 48-nm helical pitch in zero field, which increases as the helix continuously transforms into the CSL on application of an external field. The CSL and other magnetic textures [5,17–21] can be imaged using Lorentz transmission electron microscopy (LTEM).

The phase diagram of $\text{Cr}_{1/3}\text{NbS}_2$ under an external magnetic field applied perpendicular to the c axis indicates the presence of five magnetic states: paramagnetism at temperatures above the transition temperature, chiral helimagnetism

*amelia.hall@warwick.ac.uk

†g.balakrishnan@warwick.ac.uk

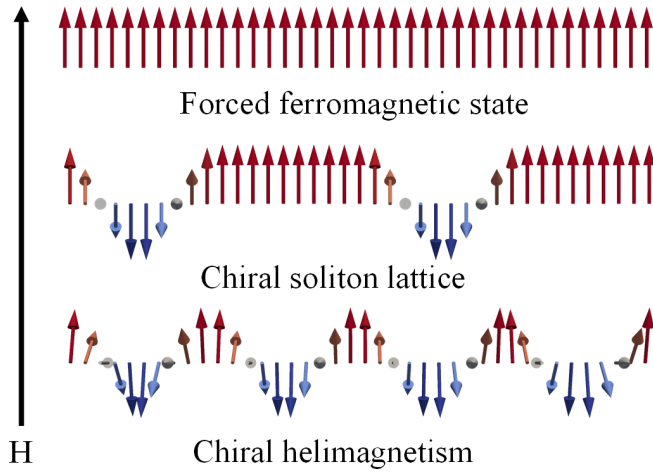


FIG. 1. Visualization of chiral helimagnetism, a chiral soliton lattice (CSL), and a forced ferromagnetic state. The arrows show the magnetic moments of each atom. As the magnetic field (H) increases, the part of each helix that is aligned with the field expands in size, increasing the period of the CSL, until finally the moments are arranged in a forced ferromagnetic state.

as the magnetic ground state, a highly helical CSL phase (CSL-1), a highly ferromagnetic CSL phase (CSL-2), and at high enough magnetic field a region of field polarized forced ferromagnetism aligned with the external magnetic field [13]. Additionally, if instead the external magnetic field is applied parallel to the c axis of the material, a chiral conical magnetic phase is produced, while at most oblique fields directed at the material there is a tilted CSL phase produced [22,23]. Some form of CSL phase is, therefore, stabilized for a large number of external field magnitudes and directions, which is an exciting prospect for device applications. In Fig. 1, examples

of chiral helimagnetism, a CSL, and the forced ferromagnetic (FFM) state are displayed.

Recently, $\text{Cr}_{1/3}\text{TaS}_2$ has been shown to form a CSL phase, showing that $\text{Cr}_{1/3}\text{NbS}_2$ is not unique among the intercalated TMDCs in this phenomenon [24]. Additionally, $\text{Mn}_{1/3}\text{NbS}_2$ has been reported as being chiral helimagnetic [25] with an ordering temperature of $T_C = 45$ K and a more recent study using neutron diffraction suggests that it was possible that $\text{Mn}_{1/3}\text{NbS}_2$ was either a ferromagnet with a small domain size of 250 nm along the c axis or a helimagnet with a modulation size far larger than the one found in $\text{Cr}_{1/3}\text{NbS}_2$ [26].

A combination of powder neutron diffraction and heat-capacity measurements have been used to suggest a change in the magnetic ordering in the material below 20 K. A magnetic field—temperature phase diagram constructed from hysteresis in magnetization measurements suggests that $\text{Mn}_{1/3}\text{NbS}_2$ might be helimagnetic at temperatures under 20 K [27]. Recent Lorentz transmission electron microscopy (LTEM) measurements of $\text{Mn}_{1/3}\text{NbS}_2$ [27] were used to support this conclusion. The 3D Heisenberg model has been applied to $\text{Mn}_{1/3}\text{NbS}_2$ and the magnetic moments were found to be short range and isotropic, allowing for coupling both within the ab plane and to the c axis [28].

In this paper, we present a detailed investigation of the magnetic properties of single crystals of both $\text{Cr}_{1/3}\text{NbS}_2$ and $\text{Mn}_{1/3}\text{NbS}_2$ using ac and dc susceptibility, as well as LTEM measurements, to probe any differences that may indicate why $\text{Mn}_{1/3}\text{NbS}_2$ does not appear to form a CSL. We also provide sufficient evidence to ascertain whether $\text{Mn}_{1/3}\text{NbS}_2$ exhibits helimagnetic ordering below its transition temperature. Establishing the correct structural space group in these crystals can often prove difficult with just single crystal x-ray diffraction techniques. Here we show how it is possible to unambiguously distinguish between the centrosymmetric and noncentrosymmetric structures using electron diffraction techniques.

II. EXPERIMENTAL DETAILS

A. Sample synthesis

Polycrystalline samples of $\text{Cr}_{1/3}\text{NbS}_2$ and $\text{Mn}_{1/3}\text{NbS}_2$ were prepared using stoichiometric amounts of Nb, S, and also Cr or Mn powders, respectively. The powders were thoroughly ground inside an argon-filled glove box, sealed in evacuated quartz tubes, and then heated at a rate of 15°C per hour to 450°C and held there for 24 hours. This heating cycle was repeated several times until most of the S had visibly reacted with the other components and the resulting powder appeared mostly black. To complete the phase formation, the quartz tubes were then slowly heated to 950°C and held there for 100 hours before being quenched in cold water. The phase purity and structural properties of these powders were checked using powder x-ray diffraction.

Single crystal samples were prepared in sealed quartz tubes by chemical vapor transport, using polycrystalline materials of the correct composition and iodine as a transport agent. The powder was slowly heated to a highest temperature of 950°C , with a temperature difference of 150°C across the tube. After three weeks, $\text{Mn}_{1/3}\text{NbS}_2$ and $\text{Cr}_{1/3}\text{NbS}_2$ crystals in the form of platelets approximately 3 mm and 1 mm along their longest

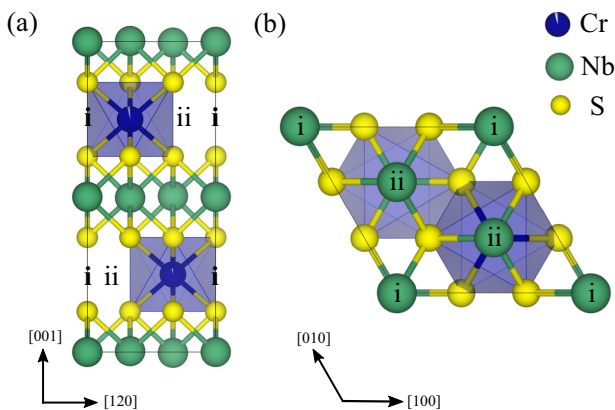


FIG. 2. Crystal structure of $\text{Cr}_{1/3}\text{NbS}_2$ viewed along (a) the a axis and (b) c axis, with S atoms shown in yellow, Nb atoms shown in green, and Cr atoms shown in blue. The occupancy of the intercalated sites is reflected by the proportion of the site shown in blue. The octahedral sites of the $2c$ Wyckoff position are shown by blue polyhedra. The projection of the $2b$ and $2d$ sites as seen from each direction are indicated using i and ii, respectively.

sides were formed, respectively. All the measurements were performed on single crystals from the same synthesis batch.

B. Single crystal x-ray diffraction

Single crystal x-ray diffraction data of $\text{Cr}_{1/3}\text{NbS}_2$ were collected for a crystal of dimensions $0.13 \times 0.12 \times 0.02 \text{ mm}^3$ using an Oxford Diffraction Gemini diffractometer, employing graphite monochromated Mo K_α radiation ($\lambda = 0.71073 \text{ \AA}$) generated by a fine-focus sealed tube Enhance x-ray source and detected by a Ruby CCD detector.

Single crystal diffraction data of $\text{Mn}_{1/3}\text{NbS}_2$ were collected for a crystal of dimensions $0.21 \times 0.14 \times 0.08 \text{ mm}^3$ using a Rigaku Oxford Diffraction Synergy diffractometer, employing mirror monochromated Mo K_α radiation ($\lambda = 0.71073 \text{ \AA}$) generated by a microfocus sealed tube PhotonJet x-ray source and detected at a HyPix hybrid photon counting detector. In both cases, the temperature was controlled using an Oxford Cryosystems Cryostream [29] at 295 and 300 K, respectively, with data collection, indexing, reduction, and absorption correction mediated using CrysAlisPRO [30]. For the Cr system, absorption was accounted for by use of an empirical, spherical harmonics approach as implemented in SCALE3 ABSPACK, while for the Mn system a Gaussian integration over a multifaceted crystal model was employed.

Structural solutions were obtained using SHELXT [31] and further refined by full-matrix least squares, using SHELXL [32], both operating through OLEX2 [33].

C. Magnetization and ac susceptibility

Magnetization measurements were performed on single crystal samples of $\text{Cr}_{1/3}\text{NbS}_2$ and $\text{Mn}_{1/3}\text{NbS}_2$ using a Quantum Design Magnetic Property Measurement System for temperatures between 1.8 and 300 K in applied magnetic fields up to 0.2 T applied both parallel and perpendicular to the c axis of the crystals. A Quantum Design Physical Property Measurement System was used for ac susceptibility measurements on single crystal samples. Measurements were performed in an ac field of 0.3 mT at frequencies between 50 Hz and 10 kHz in dc fields up to 100 mT. The samples were orientated so the magnetic fields were applied perpendicular to the c axis.

D. Electron microscopy

Two electron microscopes were used to investigate $\text{Cr}_{1/3}\text{NbS}_2$ and $\text{Mn}_{1/3}\text{NbS}_2$ single crystals. To distinguish the centrosymmetric from the noncentrosymmetric structures, measurements were made along the [001] direction of the crystals. Samples were prepared by placing small amounts of each material onto lacey carbon TEM grids. Images and selected area electron diffraction patterns were recorded using a JEOL2100 transmission electron microscope, operated at 200 kV with a Gatan OneView digital camera.

To examine the in-plane structural features of the materials, samples were instead prepared using an FEI NanoLab-600 Helios Dual-Beam focused ion beam (FIB) microscope equipped with an Omniprobe-200 micromanipulator. Single crystals of $\text{Mn}_{1/3}\text{NbS}_2$ and $\text{Cr}_{1/3}\text{NbS}_2$ were mounted inside the FIB on their (001) face and samples of approximate size

$20 \times 5 \mu\text{m}^2$ and $1 \mu\text{m}$ thickness were cut normal to this face using gallium ion milling. They were then lifted out with the micromanipulator and platinum deposition was used to attach the samples to Omniprobe grids. Further gallium ion milling was used to thin the samples to approximately 100 nm so they were electron-transparent. These samples were then measured using an FEI Titan³ 80-300 transmission electron microscope operated at an acceleration voltage of 300 kV and equipped with a high-brightness XFEG field-emission electron gun. Images were recorded on a 2048×2048 pixel CCD using either a Gatan Ultrascan 1000 camera or a Gatan 865 Tridiem camera which allows images to be energy-filtered.

In normal operation, the electromagnetic objective lens applies a 2 T field to the specimen which would force it into the magnetically saturated state. Diffraction patterns were acquired in this condition but images of the magnetic structure were acquired either in Lorentz mode where the image is formed using the Lorentz lens or in low-magnification mode where the image is formed using the diffraction lens. Neither of these lenses applies a significant field to the sample and when an applied field was required, the objective lens was weakly excited to apply a field parallel to the electron beam. The applied magnetic field corresponding to a given objective lens current had been calibrated to within 1 mT using an FEI Hall probe holder.

The defocus and magnification were calibrated by acquiring images with the same lens settings from Agar Scientific's S106 calibration specimen, which consists of lines spaced by 463 nm ruled on an amorphous film. The defocus was found by taking digital Fourier transforms of these images and measuring the radii of the dark rings that result from the contrast transfer function of the lens using the method described in Ref. [34].

III. RESULTS AND DISCUSSION

A. Single crystal x-ray diffraction

To distinguish the noncentrosymmetric $M_{1/3}\text{NbS}_2$ materials in space group $P6_322$ from the centrosymmetric $M_{1/4}\text{NbS}_2$ materials in space group $P6_3/mmc$, structural investigation techniques such as single crystal x-ray diffraction are necessary.

A representation of the model derived from single crystal x-ray diffraction data taken at room temperature for $\text{Cr}_{1/3}\text{NbS}_2$ is shown in Fig. 2. Despite a highly ambiguous Flack parameter, the structure is well-modeled in the noncentrosymmetric space group, with excellent agreement between the calculated and observed structure factors; refinement in the centrosymmetric space group $P6_3/mmc$ provides a significantly worse fit and a less simple structural model. An inversion twin law is employed in the refinement for completeness for which the twin component scale factor refines with high ambiguity to effectively zero [0.1(6)]. We find a small proportion of disorder over the main site [0.952(2)] and site i [0.048(2)].

While the same refinement is possible for the Mn phase, the true diffraction pattern exhibits a complex array of superstructure peaks along all axes. Efforts to resolve this remain

TABLE I. Atomic positions and occupancies for $\text{Cr}_{1/3}\text{NbS}_2$ and $\text{Mn}_{1/3}\text{NbS}_2$.

$\text{Cr}_{1/3}\text{NbS}_2$ ($P6_322$)					
Atom	$a = 5.7396(2)$ Å Wyckoff	$c = 12.1325(3)$ Å x	$R_1 = 2.58\%$ y	$wR_2 = 5.48\%$ z	Flack = 0.1(6) Occupancy
Cr1	2c	$\frac{1}{3}$	$\frac{2}{3}$	$\frac{1}{4}$	0.952(2)
Nb1	2a	0	0	0	1.00
Nb2	4f	$\frac{1}{3}$	$\frac{2}{3}$	0.99735(2)	1.00
S1	12i	0.33246(7)	-0.00030(8)	0.13058(3)	1.00
Cr2	2b	0	0	$\frac{1}{4}$	0.048(2)
$\text{Mn}_{1/3}\text{NbS}_2$ ($P6_322$)					
Atom	$a = 5.7933(4)$ Å Wyckoff	$c = 12.6451(7)$ Å x	$R_1 = 3.49\%$ y	$wR_2 = 11.16\%$ z	Flack = 0.57(10) Occupancy
Mn1	2c	$\frac{1}{3}$	$\frac{2}{3}$	$\frac{1}{4}$	0.851(15)
Nb1	2a	0	0	0.00000	1.000
Nb2	4f	$\frac{1}{3}$	$\frac{2}{3}$	0.50054(2)	1.000
S1	12i	0.33342(12)	0.00360(2)	0.12401(8)	1.000
Mn2	2b	0	0	$\frac{1}{4}$	0.079(15)
Mn3	2d	$\frac{2}{3}$	$\frac{1}{3}$	$\frac{1}{4}$	0.020(15)

ongoing but, for the purpose of this discussion, we acknowledge that the true structure likely forms a highly twinned approximation of that shown for $\text{Cr}_{1/3}\text{NbS}_2$ in Fig. 2 with significant breaking of the translational symmetry therein. A reconstruction of the Ewald sphere for this data set can be seen in the Supplemental Material [35]. Refinement of the known model to the aristotype peak set, i.e., the idealized high symmetry version of the low symmetry structure, yields a phase with disorder over the main site [0.851(15)], site i [0.079(15)], and site ii [0.020(15)], and potentially greater inversion twinning with a Flack parameter of 0.57(10). Despite this inaccuracy, Table I reports the statistical fits of the aristotypical model to both data sets, along with the lattice and Flack parameters, atomic positions, and site occupancies for the purpose of discussion.

Given the remaining ambiguity in the $\text{Mn}_{1/3}\text{NbS}_2$ structure and to provide more evidence for the noncentrosymmetric solution to the $\text{Cr}_{1/3}\text{NbS}_2$ data, further evidence to support noncentrosymmetry in these phases is desired. A complementary method that can be used is transmission electron microscopy.

B. Electron microscopy—structural features

Using electron diffraction along the [001] direction [see Figs. 3(a) and 3(b)] of these materials, it is possible to compare simulated kinematic diffraction patterns (i.e., assuming single scattering) of $M_{1/3}\text{NbS}_2$ to $M_{1/4}\text{NbS}_2$. The difference between the relative intensities makes it obvious whether or not the desired concentration of M (i.e., 1/3) is present. Figure 3(c) displays an example of an electron diffraction pattern taken at room temperature, measured for a $\text{Mn}_{1/3}\text{NbS}_2$ crystal, and is consistent with the simulation of the noncentrosymmetric structure.

Figure 3 also shows bright-field images and electron diffraction patterns acquired from $\text{Mn}_{1/3}\text{NbS}_2$ and $\text{Cr}_{1/3}\text{NbS}_2$ at room temperature and viewed in the [100] direction. Figure 3(d) shows the arrangement of atoms expected in this orientation and Fig. 3(e) shows a simulated kinematic diffraction pattern. The experimental diffraction patterns were taken from regions 670 nm in diameter. The pattern for $\text{Cr}_{1/3}\text{NbS}_2$ shown in Fig. 3(f) is consistent with the simulation. Bragg reflections at $00l$ are kinematically forbidden when l is odd but these appear in the experimental pattern because electrons are scattered multiple times as they pass through the specimen.

The diffraction pattern for $\text{Mn}_{1/3}\text{NbS}_2$ [Fig. 3(g)] displays superlattice reflections in addition to the expected reflections. These reflections correspond to a superlattice with a period of $3c$ in the \mathbf{c} direction and $7d_{010}$ in the \mathbf{b}^* direction, where d_{010} is the spacing of the (010) planes. This may indicate the presence of ordered Mn vacancies. The absence of a Mn atom would then allow the nearest-neighbor atoms to relax, forming a structure with a pattern similar to that shown in Fig. 3. To confirm that this is the cause of these superlattice reflections, further work to find a full structure solution for our $\text{Mn}_{1/3}\text{NbS}_2$ sample is needed.

The supercell seen in the electron diffraction is in disagreement with that found for the single-crystal x-ray diffraction, for which the pattern superficially corresponds to a doubling of all axes. This would then lead to a different ordering of the Mn vacancies. This difference could potentially be explained by the fact that the single-crystal x-ray diffraction data averages over a macroscopic sample, whereas the transmission electron diffraction data necessarily samples a small and very thin volume. This would then suggest that the period of the superlattice varies across the sample so different results are observed in localized regions when compared with an average across the whole sample. Some evidence that what we see is a local effect can be seen by comparing the pristine (030)

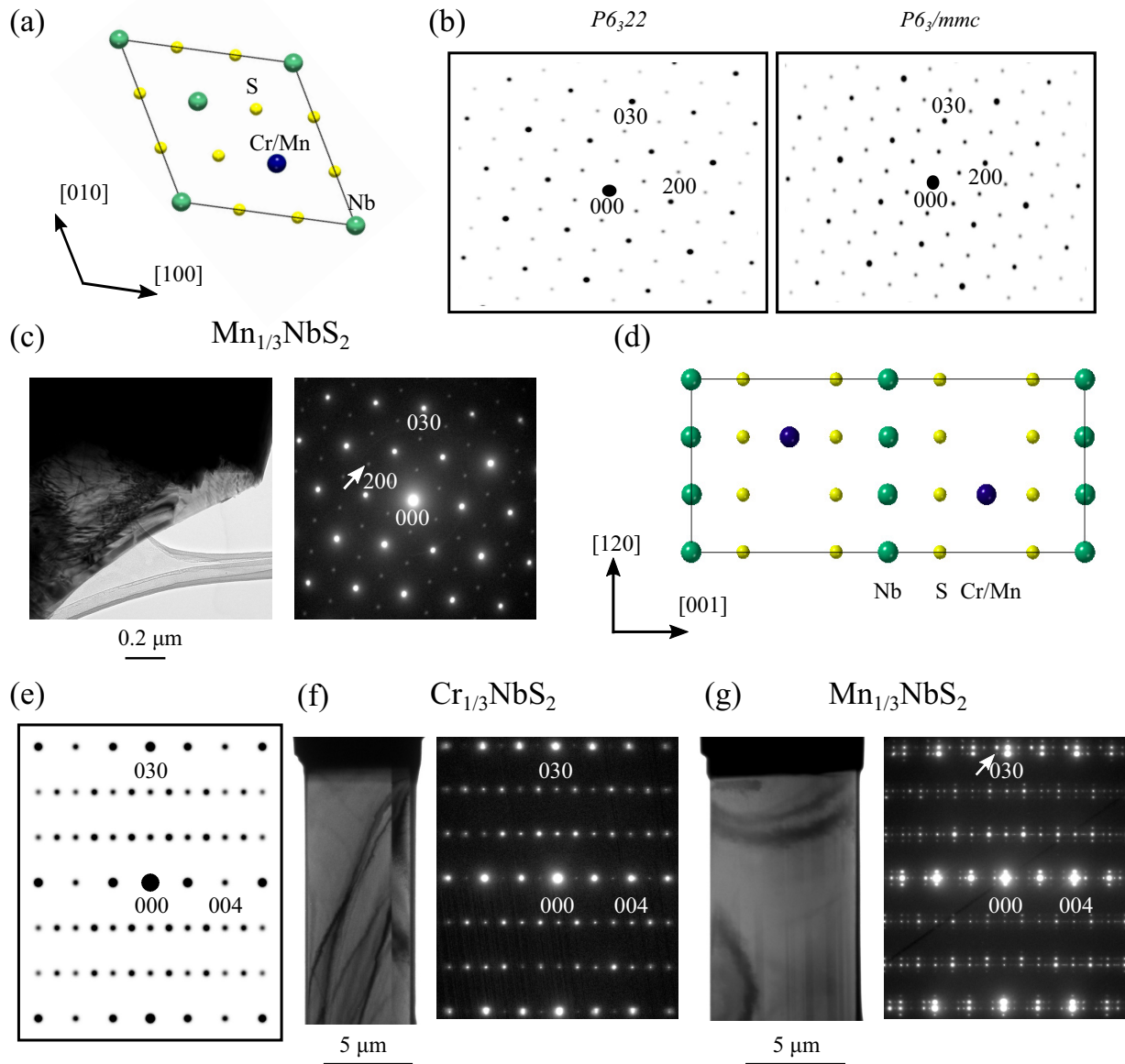


FIG. 3. (a) Unit cell of $\text{Mn}_{1/3}\text{NbS}_2$ or $\text{Cr}_{1/3}\text{NbS}_2$ viewed down the $[001]$ direction. (b) Simulated electron diffraction patterns along the $[001]$ direction for both the noncentrosymmetric $P6_322$ structure and the centrosymmetric $P6_3/mmc$ structure, which differ from each other in the relative intensities of key spots (200) and (030), assuming kinematic scattering. An electron micrograph (c) of a crystal of $\text{Mn}_{1/3}\text{NbS}_2$ and an electron diffraction pattern from the same area are shown and match well with the simulation for the $P6_322$ space group, with the especially faint (200) spot marked with an arrow. (d) The unit cell viewed along $[100]$ direction. (e) A simulation of the corresponding electron diffraction pattern. (f) Bright-field images and electron diffraction patterns from $\text{Cr}_{1/3}\text{NbS}_2$ and (g) $\text{Mn}_{1/3}\text{NbS}_2$. While the $\text{Cr}_{1/3}\text{NbS}_2$ pattern matches well with the simulation, $\text{Mn}_{1/3}\text{NbS}_2$ displays extra reflections indicating a superlattice with a period of $3c$ in the c direction and $7d_{010}$ in the b^* direction.

peak seen in Fig. 3(c) along the $[001]$ direction to the (030) peak surrounded by superlattice reflections seen along $[100]$ in Fig. 3(g).

C. Magnetization, dc, and ac susceptibility

To compare the magnetic behavior of the Cr and Mn intercalated crystals, the dc magnetization of both materials was measured at temperatures between 5 and 300 K with a field of 0.01 T applied either parallel or perpendicular to the c axis, (see Fig. 4). In the paramagnetic state, the data are isotropic and can be fitted using the Curie-Weiss law. For dc field

$H \perp c$, the Weiss temperatures of +109(2) K and +62(1) K for the Cr and Mn intercalated crystals, respectively, indicate the interactions between the magnetic ions are ferromagnetic. In the ordered state, the large difference between the magnitude of the susceptibility when the field is applied parallel or perpendicular to the c axis shows that the ordered moments strongly prefer to lie in the ab plane and that these materials are both highly anisotropic.

For $\text{Cr}_{1/3}\text{NbS}_2$, the effective magnetic moment, calculated from the Curie-Weiss law, $\mu_{\text{eff}} = 3.94(13) \mu_B/\text{Cr}$ for $H \perp c$ is within error of the quenched spin-only Cr^{3+} ($3.87 \mu_B/\text{Cr}^{3+}$).

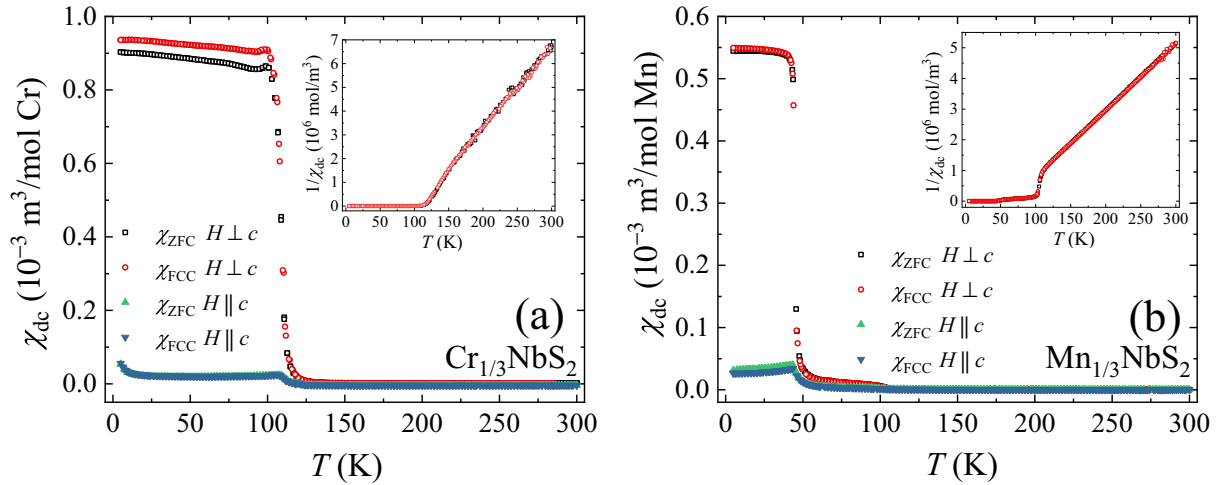


FIG. 4. Temperature dependence of the dc susceptibility $\chi_{dc}(T)$, collected in zero-field-cooled (ZFC) warming and field-cooled cooling (FCC) modes for (a) $\text{Cr}_{1/3}\text{NbS}_2$ and (b) $\text{Mn}_{1/3}\text{NbS}_2$ in an applied field of 10 mT. It is clear from the large difference between the susceptibility for each field direction that these are highly anisotropic materials, with the ab plane as the easy plane. Insets show the inverse ZFC and FCC susceptibility with $H \perp c$. For $\text{Cr}_{1/3}\text{NbS}_2$, the inverse susceptibility is shown measured in an applied field of 33 mT to increase the signal in the paramagnetic state.

An earlier report states that the Cr ions can adopt different valence states in this material [36], with the majority of the ions being Cr^{3+} but with regions in the material where the helical order is broken and the ions instead adopt the Cr^{4+} ($2.83 \mu_B/\text{Cr}^{4+}$) valence. For $\text{Mn}_{1/3}\text{NbS}_2$, $\mu_{\text{eff}} = 5.43(1) \mu_B/\text{Mn}$, for $H \perp c$ as calculated with the Curie-Weiss law. This is consistent with previous reports on this material [37] that give values for the effective moment between the spin-only moments of $4.90 \mu_B/\text{Mn}^{3+}$ and $5.92 \mu_B/\text{Mn}^{2+}$. The value may be modified by the presence of a small quantity of $\text{Mn}_{1/4}\text{NbS}_2$ within the samples [38].

Figure 4 shows that the single crystals of $\text{Cr}_{1/3}\text{NbS}_2$ order magnetically at 111 K, which is lower than the reported 130 K and can be attributed to a degree of substitutional disorder [16]. This disordered state is a possible interpretation of the single crystal diffraction data taken for $\text{Cr}_{1/3}\text{NbS}_2$. Additionally, a peak in $\chi(T)$ appears close to the transition temperature, and has been previously modeled with the chiral XY model and attributed to a commensurate-incommensurate magnetic transition [25,39,40].

A step at 100 K in the temperature dependence of the dc magnetization of the Mn-intercalated crystals is due to a small quantity of $\text{Mn}_{1/4}\text{NbS}_2$ [26,38], which orders below this temperature. The bulk of the sample ($\text{Mn}_{1/3}\text{NbS}_2$) undergoes magnetic order at 45 K.

Figure 5 shows the in-phase component of the ac susceptibility χ' and its first derivative with respect to the dc magnetic field $d\chi'/dH$, as a function of magnetic field H for $\text{Cr}_{1/3}\text{NbS}_2$ at 60 and 90 K, and for $\text{Mn}_{1/3}\text{NbS}_2$ at 10 and 36 K. Here, an ac field of 113 Hz with an amplitude of 0.3 mT is applied perpendicular to the c axis of the crystals. For $\text{Cr}_{1/3}\text{NbS}_2$, a dramatic fall in $\chi'(H)$ with increasing H marks the boundary between the helimagnetic ground state and the CSL phase, while a drop in $\chi'(H)$ (evident as a shallow minimum in $d\chi'/dH$) is present at the crossover from the helicity-rich CSL-1 phase to the more ferromagnetic

CSL-2 phase [see Figs. 5(a) and 5(b)]. This drop is more obvious at 90 K, but is still present at 60 K. The transition from the CSL-2 to the field polarized or FFM state is harder to locate, and the boundary was chosen at the point where the susceptibility ceases to change significantly with field ($d\chi'/dH = 0$).

For $\text{Mn}_{1/3}\text{NbS}_2$, all the magnetic phase boundaries are denoted by changes in gradient of $\chi'(H)$ [see Figs. 5(c) and 5(d)]. The obvious minimum visible in Fig. 5(d) denotes the I-II phase transition. The II-FFM phase boundary was chosen in the same way as the CSL-2-FFM phase boundary for $\text{Cr}_{1/3}\text{NbS}_2$.

Figure 6(a) displays the dc magnetization versus applied field measurements for $\text{Cr}_{1/3}\text{NbS}_2$ at several temperatures. It is immediately clear that the magnetization of the $\text{Cr}_{1/3}\text{NbS}_2$ sample studied here saturates at lower magnetic fields than those reported in Ref. [12]. This is consistent with our ac susceptibility measurements. The first derivative of the magnetization with respect to field at 60 and 90 K [Fig. 6(b)] can be compared with Fig. 5(b), with features in dM/dH marking the various phase boundaries appearing at fields that are in good agreement with the values extracted from the ac susceptibility data.

The dc magnetization measurements as a function of field for $\text{Mn}_{1/3}\text{NbS}_2$ are shown in Figs. 6(c) and 6(d). These data correspond well with our ac susceptibility measurements, with clear features in dM/dH marking potential phase boundaries. The $M(H)$ curves shown here differ in several important respects from those reported earlier [26–28], as discussed in the Supplemental Material [35].

The magnetic field–temperature phase diagrams for $\text{Cr}_{1/3}\text{NbS}_2$ and $\text{Mn}_{1/3}\text{NbS}_2$ constructed using ac susceptibility versus field measurements at fixed temperatures, similar to those shown in Fig. 5, are displayed in Fig. 7. Note, measurements of ac susceptibility versus temperature in fixed applied magnetic field are shown in the Supplemental Material [35]

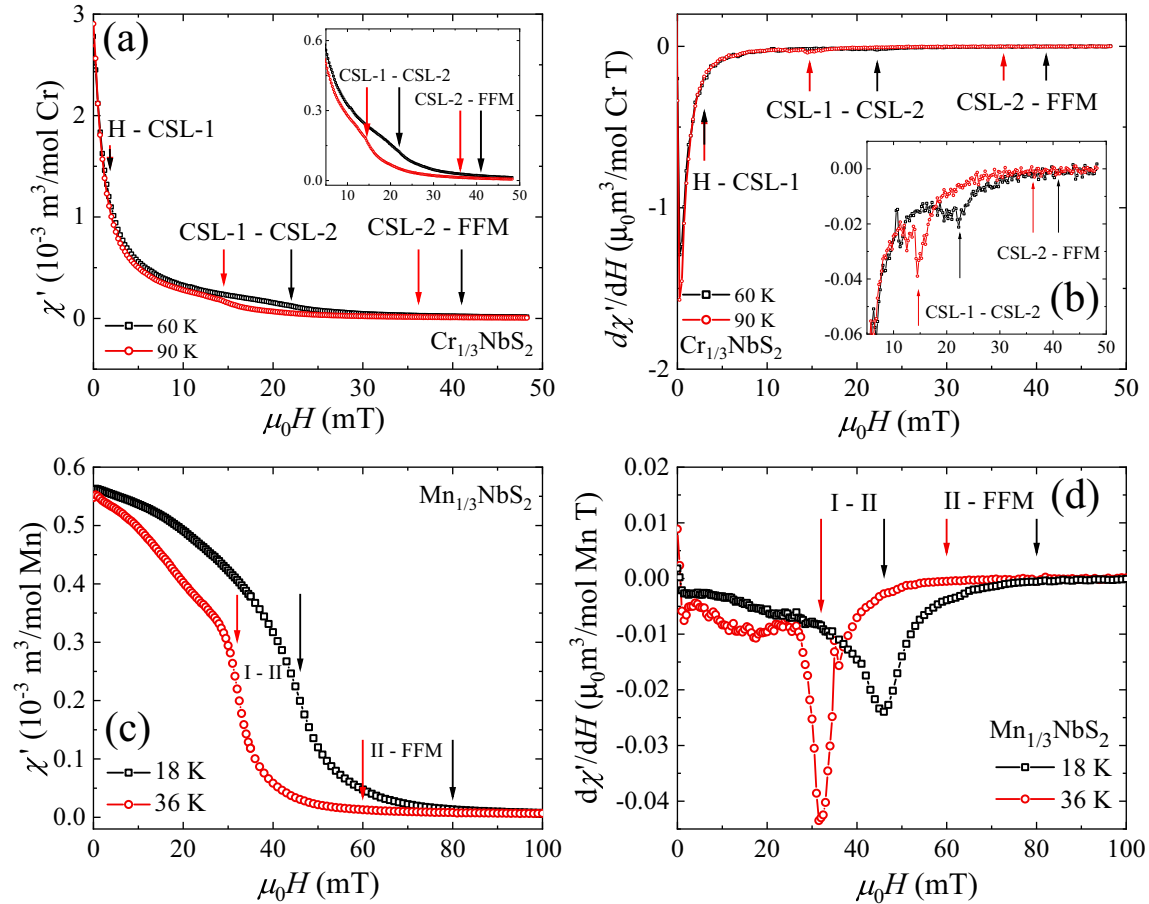


FIG. 5. (a) In-phase component of the ac susceptibility χ' as a function of dc field H directed perpendicular to the c axis and (b) $d\chi'/dH$ versus dc field H at 60 and 90 K for $\text{Cr}_{1/3}\text{NbS}_2$. Insets show the same data between 5 and 50 K, on a scale to better compare with the $\text{Mn}_{1/3}\text{NbS}_2$ data. The features used to define magnetic phase boundaries are marked by the arrows. (c) In-phase component of the ac susceptibility χ' as a function of dc field H directed perpendicular to the c axis and (d) $d\chi'/dH$ versus dc field H at 18 and 36 K for $\text{Mn}_{1/3}\text{NbS}_2$. The features used to define the magnetic phase boundaries are marked by the arrows. All the measurements were performed in an ac field of 0.3 mT at a frequency of 113 Hz.

and are consistent with the phase diagrams presented here. For both materials, the temperatures of the transitions from a paramagnetic to a magnetically ordered state are in good agreement with those obtained from dc susceptibility. The transitions present in the ordered state for $\text{Cr}_{1/3}\text{NbS}_2$ occur at significantly lower magnetic fields than previously reported [13], while the boundary in the phase diagram for $\text{Mn}_{1/3}\text{NbS}_2$ marking the entry to a FFM phase is shifted to higher fields [28]. This highlights the sensitivity of the magnetic response of these materials to disorder [16].

Five different magnetic phases can be seen in the $\text{Cr}_{1/3}\text{NbS}_2$ material [Figs. 7(a) and 7(b)], which correspond well to the helimagnetic (H), CSL-1, CSL-2, FFM, and paramagnetic (PM) phases established in previous literature [13]. The helical phase coincides with a maximum in χ' at zero field. χ' initially falls rapidly under the application of a dc magnetic field. Clear changes in χ' and/or $d\chi'/dH$ delineate the other phase boundaries. There is also a significant increase in the imaginary susceptibility at low fields, at all temperatures up to the onset of magnetic order at 111 K. This is further evidence for the chiral helimagnetic state in $\text{Cr}_{1/3}\text{NbS}_2$. χ''

also shows a large pocket of intensity that begins just below the ordering temperature in low dc magnetic fields and extends in an arc up to 25 mT at 60 K. This feature is reduced in intensity at higher frequency (see Supplemental Material [35]). There are several possible reasons for this feature, for example, the creation and destruction of novel phenomena such as the CSL. Alternatively, this signal could be explained by effects such as domain wall motion and pinning by defects, which are especially prevalent in layered materials like these.

The H - T phase diagram for $\text{Mn}_{1/3}\text{NbS}_2$ can be divided into four regions. In addition to the paramagnetic and FFM regions, there is evidence in the ac (and dc) susceptibility for two phases labeled as I and II appearing in the ordered state [see Figs. 7(c) and 7(d)]. χ' and χ'' are both significantly reduced in low dc fields compared to $\text{Cr}_{1/3}\text{NbS}_2$, indicating that the helimagnetic state is absent in $\text{Mn}_{1/3}\text{NbS}_2$. Once again, the imaginary component of the susceptibility χ'' , shows a large pocket of intensity just below the ordering temperature in low magnetic fields that cuts through the center of the phase boundary separating regions I and II. χ'' is reduced in intensity as the measuring frequency increases but is still

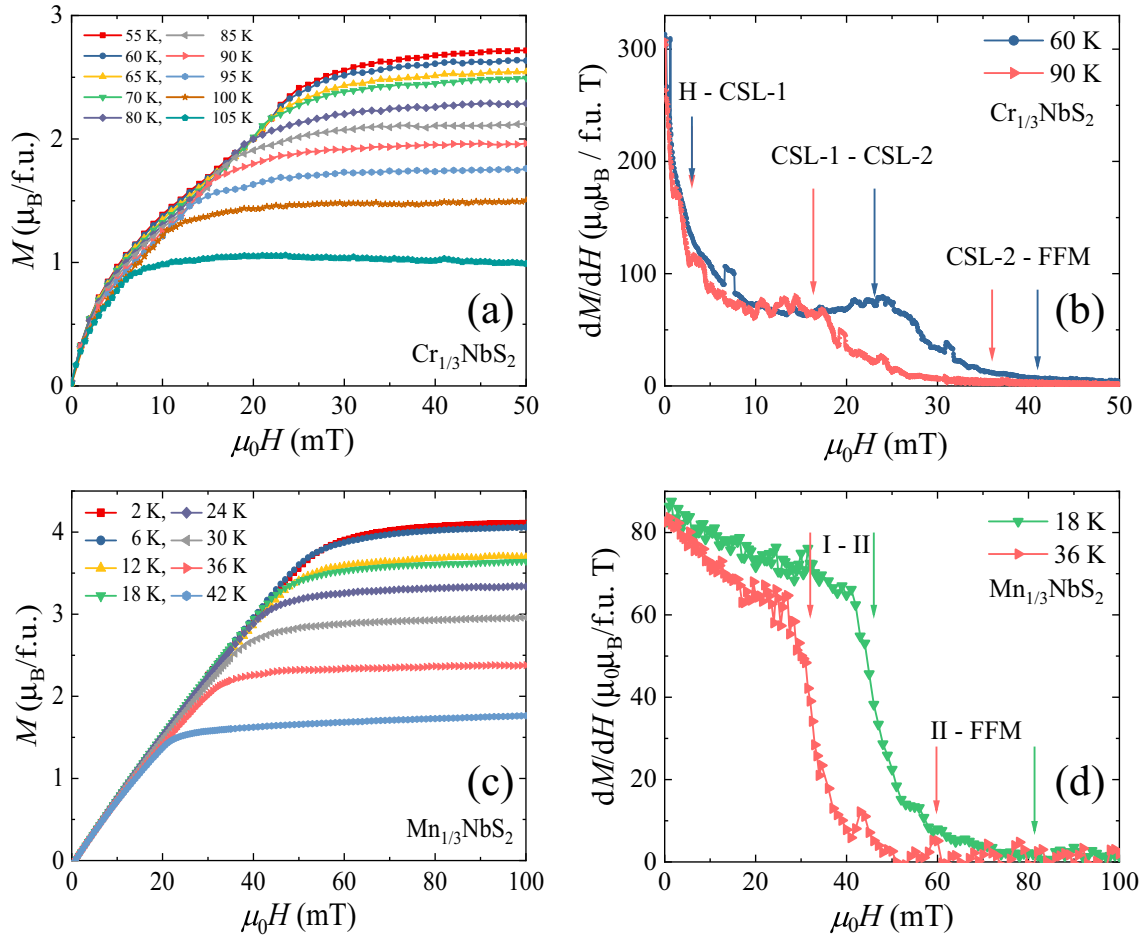


FIG. 6. (a) Magnetization M as a function of magnetic field H directed perpendicular to the c axis for different temperatures and (b) dM/dH versus magnetic field at 60 and 90 K for $\text{Cr}_{1/3}\text{NbS}_2$. The magnetic phase boundaries are marked with either blue (60 K) or red (90 K) arrows. (c) Magnetization M as a function of magnetic field H directed perpendicular to the c axis for several temperatures and (d) dM/dH versus magnetic field at 18 and 36 K for $\text{Mn}_{1/3}\text{NbS}_2$. The magnetic phase boundaries are marked by the arrows.

clearly present at 10 kHz (see Supplemental Material [35]). This signal is most likely due to domain wall motion and pinning by defects.

The exact nature of phases I and II are unknown. In fact, it seems most likely that the features seen that mark these phase boundaries are due to the motion of magnetic domains, though it is also possible that the material experiences two noncollinear magnetic phases before the moments become field polarized, neither of which were visible in the LTEM measurements. An alternative phase diagram for $\text{Mn}_{1/3}\text{NbS}_2$ with helimagnetic and CSL phases [28] was based on initial magnetization versus field curves that contain a point of inflection and hysteresis. These features are not seen in similar data collected for our crystals. Reference [27] proposed a helical phase at low field and low temperature, separated from a nearly ferromagnetic phase at higher temperatures by an almost vertical phase boundary at ~ 20 K that coincides with the disappearance of hysteresis in the $M(H)$ curves. Our measurements provide no evidence for such a phase boundary below 20 K in these crystals of $\text{Mn}_{1/3}\text{NbS}_2$, although there is a significant increase in the losses in phase I, reflected by an increase in $\chi''(T)$, as the ac measuring frequency increases (see Supplemental Material [35]). The form of the boundary

between phase II and the FMM phase matches qualitatively with the boundary shown in Ref. [27], albeit, as noted above, at lower fields.

D. Electron microscopy—magnetic features

Images acquired using transmission electron microscopy allow the projected B field to be calculated. This is the component of the magnetic flux density normal to the electron beam, averaged through the thickness of the sample.

Figure 8 shows the magnetic features observed in both samples by transmission electron microscopy. $\text{Mn}_{1/3}\text{NbS}_2$ [Fig. 8(a)] showed conventional magnetic domains separated by 180° domain walls with the magnetization lying in the (100) plane and oriented in the $[120]$ (\mathbf{b}^*) direction. Images were acquired to search for chiral solitons throughout the range of field and temperature identified in Fig. 7(d), but nothing other than conventional magnetism was observed.

Our LTEM observations are consistent with those reported in Ref. [27]. However, while this reference interprets these images as showing helimagnetism and magnetic solitons, we believe that the images obtained show that these are magnetic domains separated by 180° domain walls. The

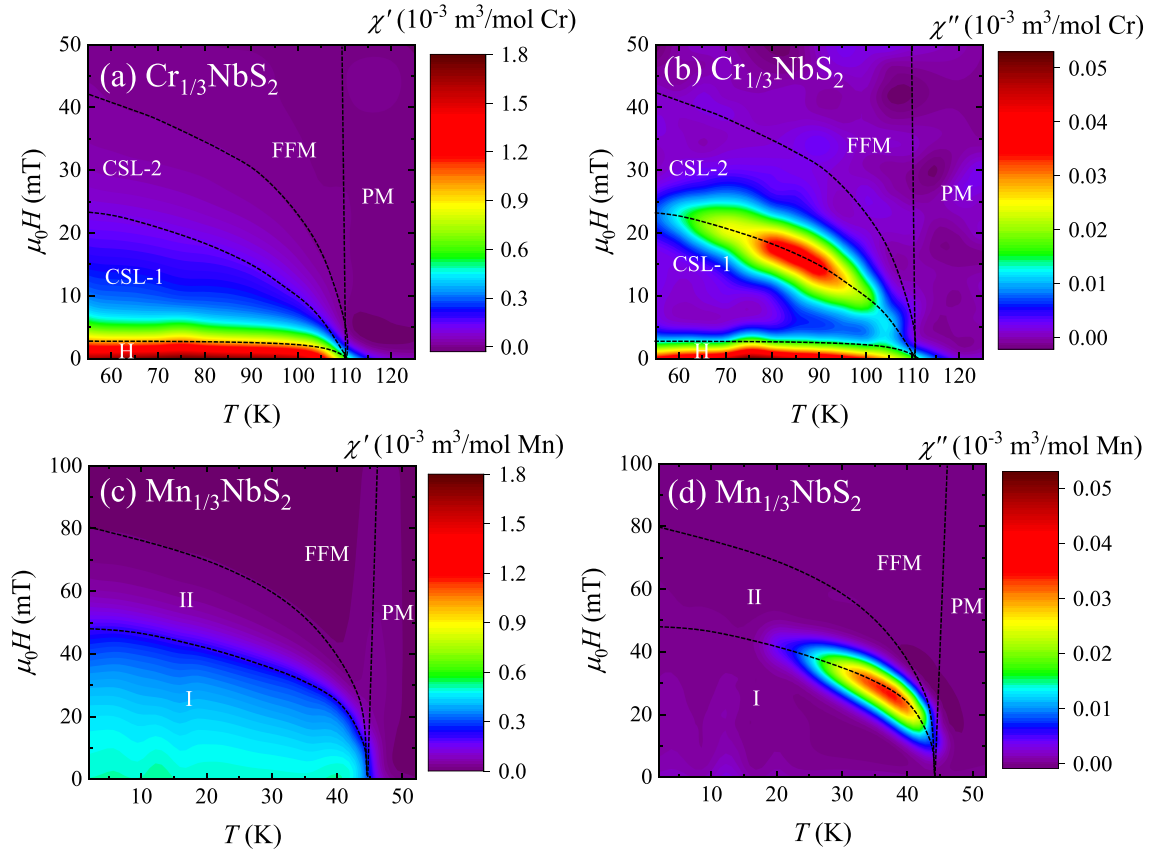


FIG. 7. (a) In-phase χ' and (b) out-of-phase χ'' components of the ac susceptibility of $\text{Cr}_{1/3}\text{NbS}_2$ as a function of temperature and dc applied field. (c) In-phase and (d) out-of-phase χ' components of the ac susceptibility of $\text{Mn}_{1/3}\text{NbS}_2$ as a function of temperature and dc applied field. For both measurements, the ac and dc magnetic fields were applied perpendicular to the c axis. Guides to the eye have been added to the phase diagrams based on features present in the data to distinguish separate phases: the helimagnetic (H), high-helicity CSL-1, highly ferromagnetic CSL-2, forced ferromagnetic (FFM), and paramagnetic (PM) phases in $\text{Cr}_{1/3}\text{NbS}_2$ and the I, II, FFM, and PM phases in $\text{Mn}_{1/3}\text{NbS}_2$ (as discussed in the text).

domains observed in our measurements vary between ~ 250 nm along the c axis, as previously observed in other work [26], and several micrometers in length. Due to the multiple phases seen in the ac susceptibility phase diagram for $\text{Mn}_{1/3}\text{NbS}_2$ [Fig. 7(c)] and the pockets of high χ'' seen in Figs. 7(b) and 7(d) for $\text{Cr}_{1/3}\text{NbS}_2$ and $\text{Mn}_{1/3}\text{NbS}_2$, respectively, it is possible that $\text{Mn}_{1/3}\text{NbS}_2$ has a noncollinear aspect to its magnetism in phases I and II that is not visible in our LTEM measurements, but the features that have been used to mark these phase boundaries can also be attributed to the rearrangement of magnetic domains.

Instead of conventional magnetic domains, $\text{Cr}_{1/3}\text{NbS}_2$ [Figs. 8(b) and 8(c)] shows thin magnetic strips. Unlike the soliton lattice reported by Togawa *et al.* [5], the strips do not show a constant periodicity and their width varies between 25 and 65 nm. The magnetization within these strips points mainly parallel or antiparallel to [120] but some of the strips appear dark, indicating the magnetization is oriented out of the plane of the sample. The fact that the periodicity is not constant is likely to be a consequence of disorder in the crystal structure, which also results in the decrease in the field value at which magnetic phase transitions occur, as well as the transition temperature.

IV. SUMMARY

Single crystals of $\text{Mn}_{1/3}\text{NbS}_2$ and $\text{Cr}_{1/3}\text{NbS}_2$ have been produced and established as crystallizing in the $P6_322$ space group. In Mn-Nb-S and Cr-Nb-S materials, it is possible to use single crystal x-ray diffraction measurements and solve the aristotype structure in either the centrosymmetric or noncentrosymmetric form. While the noncentrosymmetric space group $P6_322$ provides a discernibly better fit to the data, further evidence in support of this is provided using electron diffraction. These electron diffraction measurements show additional superlattice reflections in $\text{Mn}_{1/3}\text{NbS}_2$ when compared to the simulated pattern, while for $\text{Cr}_{1/3}\text{NbS}_2$ the diffraction data match well with the simulated pattern. A similar yet distinctly different phenomenon is observed in single crystal x-ray diffraction data and efforts to properly resolve the true nature of this superstructure are ongoing. The dc susceptibility measurements show that $\text{Cr}_{1/3}\text{NbS}_2$ and $\text{Mn}_{1/3}\text{NbS}_2$ order magnetically below $T_C = 111$ K and $T_C = 45$ K, respectively. The small step observed at 100 K in the dc susceptibility in $\text{Mn}_{1/3}\text{NbS}_2$, which coincides with the T_C expected for the $\text{Mn}_{1/4}\text{NbS}_2$ composition, supports our interpretation that these materials are prone to regions of Mn-deficiency.

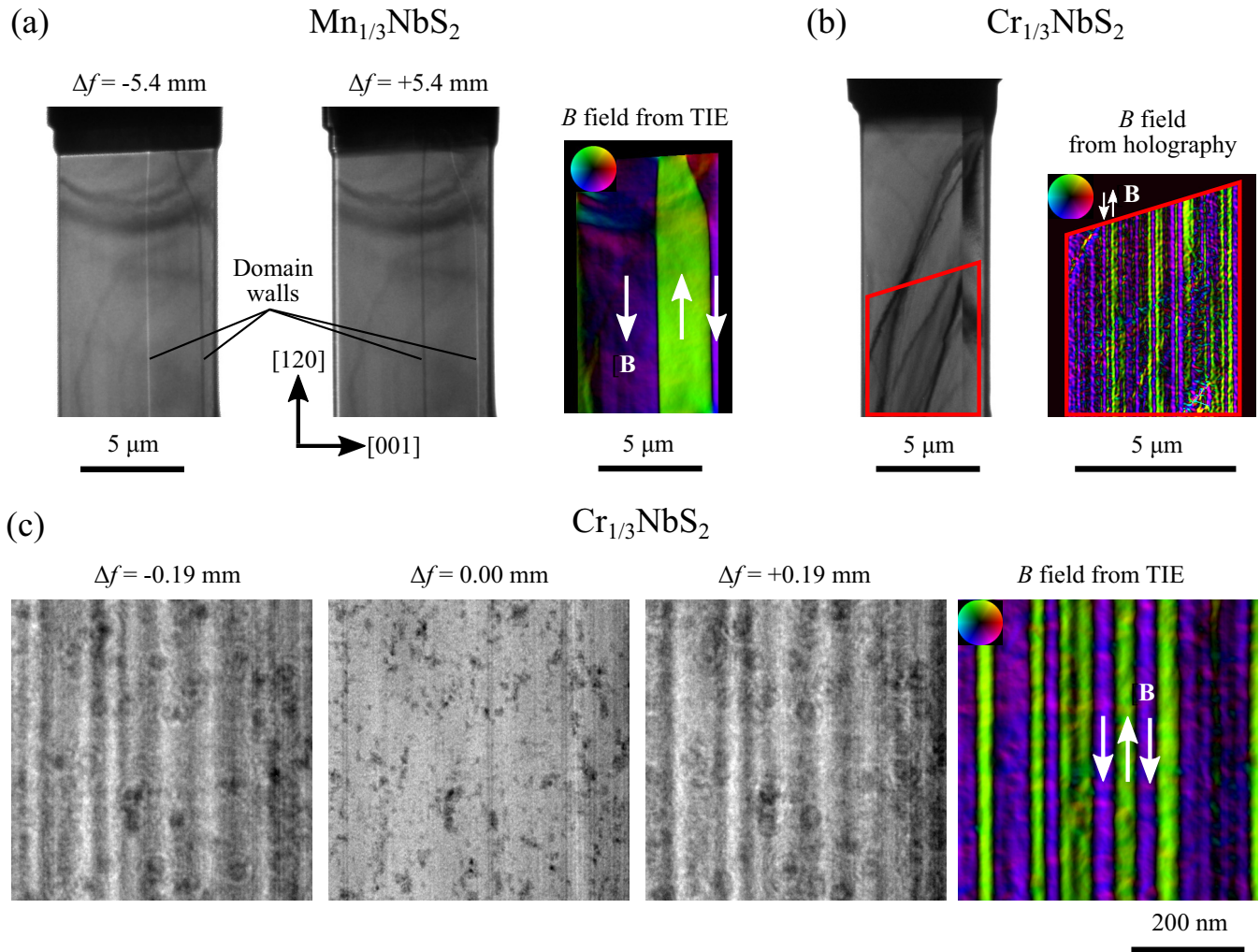


FIG. 8. (a) Transmission electron micrographs acquired from $\text{Mn}_{1/3}\text{NbS}_2$ at 35 K in a field of 63 mT, applied normal to the plane of the specimen. Images acquired under and overfocus are shown together with the projected B field reconstructed from these using the transport of intensity equation (TIE). White arrows and colors indicate the direction of the B field according to the inset color wheel. (b) An infocus image from $\text{Cr}_{1/3}\text{NbS}_2$ together with the projected B field at 92 K in zero applied field obtained using off-axis holography from the area outlined in red. Holography was used as the closely spaced magnetic features were difficult to discern with defocused imaging at this magnification. (c) Higher magnification images from $\text{Cr}_{1/3}\text{NbS}_2$ obtained at 91 K in zero applied field showing the specimen underfocus, infocus, and overfocus as well as the projected B field reconstructed from these images using the transport of intensity equation.

The magnetic field–temperature phase diagrams for $\text{Cr}_{1/3}\text{NbS}_2$ and $\text{Mn}_{1/3}\text{NbS}_2$ are mapped with ac susceptibility, with five phases identified in $\text{Cr}_{1/3}\text{NbS}_2$ and four phases in $\text{Mn}_{1/3}\text{NbS}_2$. One key difference between the two materials is that in $\text{Cr}_{1/3}\text{NbS}_2$ a region of high intensity in χ' and χ'' is observed at low magnetic fields for all temperatures below the transition temperature, which corresponds to the continuous transformation of the helimagnetic ground state to the CSL phase. This feature is notably absent for $\text{Mn}_{1/3}\text{NbS}_2$.

Lorentz transmission electron microscopy measurements reveal that while $\text{Cr}_{1/3}\text{NbS}_2$ shows the expected chiral helimagnetism, in $\text{Mn}_{1/3}\text{NbS}_2$ there is only conventional ferromagnetic behavior with visible domain walls that are consistent with those reported previously [27]. We can therefore conclude that the features seen in the ac susceptibility

measurements of $\text{Mn}_{1/3}\text{NbS}_2$ are likely due to the motion of magnetic domains rather than phase changes from non-collinear magnetism not visible in LTEM measurements and cannot be explained as being due to a helimagnetic ground state. Further careful investigations at the various magnetic features identified in $\text{Mn}_{1/3}\text{NbS}_2$ phase diagram may be necessary to understand fully why $\text{Mn}_{1/3}\text{NbS}_2$ does not exhibit helimagnetism or a CSL.

ACKNOWLEDGMENTS

This work was financially supported by the EPSRC (Grant No. EP/N032128/1 and, for J.P.T., Grant No. EP/S027106/1) We would like to acknowledge the efforts of Thomas Orton and Patrick Ruddy for their technical support.

- [1] I. Dzyaloshinsky, *J. Phys. Chem. Solids* **4**, 241 (1958).
- [2] T. Moriya, *Phys. Rev.* **120**, 91 (1960).
- [3] P. Bak and M. H. Jensen, *J. Phys. C: Solid State Phys.* **13**, L881 (1980).
- [4] S. Seki and M. Mochizuki, *Skyrmions in Magnetic Materials* (Springer International Publishing, New York, 2016)
- [5] Y. Togawa, T. Koyama, K. Takayanagi, S. Mori, Y. Kousaka, J. Akimitsu, S. Nishihara, K. Inoue, A. S. Ovchinnikov, and J. Kishine, *Phys. Rev. Lett.* **108**, 107202 (2012).
- [6] G. W. Paterson, T. Koyama, M. Shinozaki, Y. Masaki, F. J. T. Goncalves, Y. Shimamoto, T. Sogo, M. Nord, Y. Kousaka, Y. Kato, S. McVitie, and Y. Togawa, *Phys. Rev. B* **99**, 224429 (2019).
- [7] Y. Togawa, T. Koyama, Y. Nishimori, Y. Matsumoto, S. McVitie, D. McGrouther, R. L. Stamps, Y. Kousaka, J. Akimitsu, S. Nishihara, K. Inoue, I. G. Bostrem, V. E. Sinitsyn, A. S. Ovchinnikov, and J. Kishine, *Phys. Rev. B* **92**, 220412(R) (2015).
- [8] S. S. P. Parkin, M. Hayashi, and M. Thomas, *Science* **320**, 190 (2008).
- [9] J. M. van den Berg and P. Cossee, *Inorganica Chimica Acta* **2**, 143 (1968).
- [10] A. E. Hall, D. D. Khalyavin, P. Manuel, D. A. Mayoh, F. Orlandi, O. A. Petrenko, M. R. Lees, and G. Balakrishnan, *Phys. Rev. B* **103**, 174431 (2021).
- [11] K. Lu, D. Sapkota, L. DeBeer-Schmitt, Y. Wu, H. B. Cao, N. Mannella, D. Mandrus, A. A. Aczel, and G. J. MacDougall, *Phys. Rev. Mater.* **4**, 054416 (2020).
- [12] Y. Togawa, Y. Kousaka, K. Inoue, and J. Kishine, *J. Phys. Soc. Jpn.* **85**, 112001 (2016).
- [13] K. Tsuruta, M. Mito, H. Deguchi, J. Kishine, Y. Kousaka, J. Akimitsu, and K. Inoue, *Phys. Rev. B* **93**, 104402 (2016).
- [14] Y. Kousaka, T. Ogura, J. Zhang, P. Miao, S. Lee, S. Torii, T. Kamiyama, J. Campo, K. Inoue, and J. Akimitsu, *J. Phys.: Conf. Ser.* **746**, 012061 (2016).
- [15] Y. Cao, Z. Huang, Y. Yin, H. Xie, B. Liu, W. Wang, C. Zhu, D. Mandrus, L. Wang, and W. Huang, *Mater. Today Adv.* **7**, 100080 (2020).
- [16] V. Dyadkin, F. Mushenok, A. Bosak, D. Menzel, S. Grigoriev, P. Pattison, and D. Chernyshov, *Phys. Rev. B* **91**, 184205 (2015).
- [17] T. Ma, A. K. Sharma, R. Saha, A. K. Srivastava, P. Werner, P. Vir, V. Kumar, C. Felser, and S. S. P. Parkin, *Adv. Mater.* **32**, 2002043 (2020).
- [18] Y. Tokunaga, X. Z. Yu, J. S. White, H. M. Rønnow, D. Morikawa, Y. Taguchi, and Y. Tokura, *Nat. Commun.* **6**, 7638 (2015).
- [19] K. Chai, Z.-A. Li, R. Liu, B. Zou, M. Farle, and J. Li, *Nanoscale* **12**, 14919 (2020).
- [20] S. McVitie, S. Hughes, K. Fallon, S. McFadzean, D. McGrouther, M. Krajnak, W. Legrand, D. Maccariello, S. Collin, K. Garcia, N. Reyren, V. Cros, A. Fert, K. Zeissler, and H. C. Marrows, *Sci. Rep.* **8**, 5703 (2018).
- [21] J. J. Chess, S. A. Montoya, E. E. Fullerton, and B. J. McMorran, *AIP Adv.* **7**, 056807 (2017).
- [22] J. I. Yonemura, Y. Shimamoto, T. Kida, D. Yoshizawa, Y. Kousaka, S. Nishihara, Francisco Jose Trindade Goncalves, J. Akimitsu, K. Inoue, M. Hagiwara, and Y. Togawa, *Phys. Rev. B* **96**, 184423 (2017).
- [23] D. A. Mayoh, J. Bouaziz, A. E. Hall, J. B. Staunton, M. R. Lees, and G. Balakrishnan, *Phys. Rev. Research* **4**, 013134 (2022).
- [24] D. Obeysekera, K. Gamage, Y. Gao, S.-W. Cheong, and J. Yang, *Adv. Electron. Mater.* **7**, 2100424 (2021).
- [25] Y. Kousaka, Y. Nakao, J. Kishine, M. Akita, K. Inoue, and J. Akimitsu, *Nucl. Instrum. Methods Phys. Res., Sec. A* **600**, 250 (2009).
- [26] S. K. Karna, F. N. Womack, R. Chapai, D. P. Young, M. Marshall, W. Xie, D. Graf, Y. Wu, H. Cao, L. DeBeer-Schmitt, P. W. Adams, R. Jin, and J. F. DiTusa, *Phys. Rev. B* **100**, 184413 (2019).
- [27] S. K. Karna, M. Marshall, W. Xie, L. DeBeer-Schmitt, D. P. Young, I. Vekhter, W. A. Shelton, A. Kovács, M. Charilaou, and J. F. DiTusa, *Nano Lett.* **21**, 1205 (2021).
- [28] Y. Dai, W. Liu, Y. Wang, J. Fan, L. Pil, L. Zhang, and Y. Zhang, *J. Phys.: Condens. Matter* **31**, 195803 (2019).
- [29] J. Cosier and A. M. Glazer, *J. Appl. Crystallogr.* **19**, 105 (1986).
- [30] Rigaku Oxford Diffraction, *CrysAlis PRO* (Oxford Diffraction Ltd., Yarnton, UK, 2019).
- [31] G. M. Sheldrick, *Acta. Crystallogr. A Found. Adv.* **71**, 3 (2015).
- [32] G. M. Sheldrick, *Acta. Crystallogr. C Struct. Chem.* **71**, 3 (2015).
- [33] O. V. Dolomanov, L. J. Bourhis, R. J. Gildea, J. A. K. Howard, and H. Puschmann, *J. Appl. Crystallogr.* **42**, 339 (2009).
- [34] D. B. Williams and C. B. Carter, *Transmission Electron Microscopy*, 2nd ed. (Springer, New York, 2009), Chap. 28.
- [35] See Supplemental Material at <http://link.aps.org/supplemental/10.1103/PhysRevMaterials.6.024407> for additional ac susceptibility versus temperature data sets collected in different dc applied fields and ac frequencies.
- [36] V. V. Ogoblichev, Y. V. Piskunov, and F. B. Mushenok, *J. Exp. Theor. Phys.* **125**, 317 (2017).
- [37] S. S. P. Parkin and R. H. Friend, *Philos. Mag. B* **41**, 65 (1980).
- [38] Y. Ōnuki, K. Ina, T. Hirai, and T. Komatsubara, *J. Phys. Soc. Jpn.* **55**, 347 (1986).
- [39] J. Kishine, K. Inoue, and Y. Yoshida, *Prog. Theor. Phys. Suppl.* **159**, 82 (2005).
- [40] Y. Kousaka, S. Yano, J. Kishine, Y. Yoshida, K. Inoue, K. Kikuchi, and J. Akimitsu, *J. Phys. Soc. Jpn.* **76**, 123709 (2007).